Preprint of an article published in Functional Materials Letters, Volume 17, Issue 04, 2024, 2451018.

https://doi.org/10.1142/S1793604724510184

© copyright World Scientific Publishing Company

https://www.worldscientific.com/worldscinet/fml

Influence of 2D $Cu_xAl_{(100-x)}$ electrodes on the $Cu_xAl_{(100-x)}/Cu_{21}(SiO_2)_{79}$/W memristive device

Bin Gu, Guangyu Wen, Bo Zhang*
College of Physics, Hebei Normal University, Shijiazhuang 050024, China
Jhonatan Rodriguez-Pereira, Tomas Wagner*

Center of Materials and Nanotechnologies, Faculty of Chemical Technology, University of Pardubice, nam. Cs. Legii 565, Pardubice 53002, Czech Republic and Department of General and Inorganic Chemistry, Faculty of Chemical Technology, University of Pardubice, Studentska 573, 532 10 Pardubice, Czech Republic

In recent years, 2D metal nanomaterials have emerged as a novel class of 2D materials owing to their unique physiochemical properties. In this paper, memristive devices ($Cu_xAl_{(100-x)}$(BE)/$Cu_{21}(SiO_2)_{79}$/W(TE)) were fabricated utilizing 2D $Cu_xAl_{(100-x)}$ materials with different compositions as electrodes. After exfoliation by sonication, the minimum thickness of the freestanding single layer of 2D CuxAl(100-x) was only 1.5 nm. Furthermore, the distribution of SET thresholds was determined by the composition of the 2D $Cu_xAl_{(100x)}$ materials. The results suggest that the SET and RESET thresholds can be adjusted according to the composition of the 2D $Cu_xAl_{(100-x)}$ materials. The application of 2D metals as electrodes is promising for miniature memristive devices.

Keywords: 2D materials, memristive device

1. The Main Text

1 Introduction

Memristive devices are promising candidates for next-generation memory. [1,2] The mechanism of memristive devices has been explained using many models, such as the electrochemical metallization model (ECM), the valence change model (VCM), the thermochemical model, the phase change memory model, the magnetresistive model, and the ferroelectric model. [3] The basic structure of a memristive device includes an insulating electrolyte layer and metal electrodes. The resistance of memristive devices reflects the cyclic formation and dissolution of conductive filaments in the SET and RESET processes. [4] Nevertheless, the SET and RESET thresholds are related to various factors, such as the electrolyte material, electrode material, and algorithm. [5]

2D materials present many unique properties and have been widely applied in the fabrication of memristive devices. [6] For instance, graphene oxide has been reported as an electrode material for reducing power consumption. [7] Graphene can be used as a blocking layer to restrict ion migration. [8,9] In previous studies [10–12], we developed a new method to fabricate 2D materials via the physical vapor deposition method. A 2D stack of single GeSe layers was first synthesized by thermal evaporation. [11] However, the mechanism underlying the formation of the 2D structure is unclear, and our recent findings suggest that this phenomenon might be related to the thermal expansion of the substrate. [13] Among all the 2D materials synthesized via magnetron sputtering, inert 2D tungsten could be utilized as an electrode or interconnect in memristive devices. [10]

$Cu_xAl_{(100-x)}$ alloys are intensively studied for use as interconnects in integrated circuits due to their resistance to electromigration. [14,15] Electromigration is a common transport phenomenon that causes the formation of hillocks and whiskers. [16] Cu additives are often used to harden light and soft Al. [17] Since the structure of metals and alloys is usually considered energetically favorable in three dimensions (3D) rather than in 2D, the preparation of 2D metals with large lateral dimensions is rather difficult. Many different methods, including CVD and hydrothermal methods, have been employed to synthesize 2D metals. Therefore, 2D metals are rarely applied in the field of memristive devices. In this paper, we prepared memristive devices with the structure of $Cu_xAl_{(100-x)}$ (top electrode referred to as TE)/$Cu_{21}(SiO_2)_{79}$/W (bottom electrode referred to as BE), in which the electrodes and electrolyte were synthesized as 2D materials. Furthermore, the SET and RESET thresholds can be regulated according to the composition of the $Cu_xAl_{(100-x)}$ electrode. Therefore, 2D metals, especially those with ultrathin single layers, show promising application as electrodes for memristive devices.

2 Results and discussion

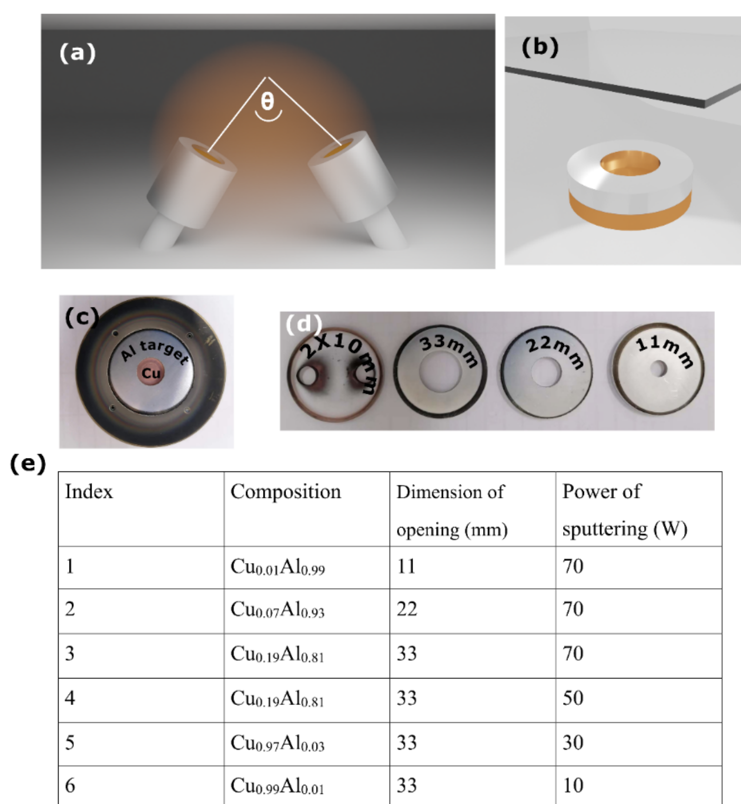

Index	Composition	Dimension of opening (mm)	Power of sputtering (W)
1	$Cu_{0.01}Al_{0.99}$	11	70
2	$Cu_{0.07}Al_{0.93}$	22	70
3	$Cu_{0.19}Al_{0.81}$	33	70
4	$Cu_{0.19}Al_{0.81}$	33	50
5	$Cu_{0.97}Al_{0.03}$	33	30
6	$Cu_{0.99}Al_{0.01}$	33	10

Figure 1 (a) Illustrative image of the conventional confocal cosputtering technique; (b) illustrative image of the targets with openings where the two targets (Cu and Al) were vertically aligned; (c) image of the assembled targets; (d) appearance of SiO_2 and Cu targets; (e) composition of $Cu_xAl_{(100-x)}$ depending on the power and size of the openings where the numbers represent the size of openings.

The SiO_2 layer is an epitaxial layer with good CMOS compatibility and has been widely used as the electrolyte layer

of memristive devices. [18] Since SiO_2 is an insulator, the SiO_2 electrolyte layer must be thin enough to allow the formation of conductive filaments. Furthermore, the formation of filaments also relies on the catalysis of electrodes, for instance, Pd or Pt. [19] Nevertheless, the high cost of such noble metal electrodes restricts their industrial application. In addition to pure SiO_2, Ag- or Cu-doped SiO_2, as the electrolyte layer, is also used in memristive devices. [20] The cosputtering technique is the most common method for Ag or Cu doping. [21]Conventional confocal cosputtering requires two guns placed at a specific angle, as shown in Figure 1(a). Nevertheless, materials deposited at an oblique angle commonly present various morphologies, such as column and helix structures. [22] In this paper, a Cu-doped electrolyte and a $Cu_xAl_{(100-x)}$ electrode were sputtered with special targets, as shown in Figure 1(b)-(d). Specifically, to achieve a thin film with two components, the Al target and Cu target were placed vertically using this method, as shown in Figure 1 (b), where the topmost target comprises openings, as described in Figure S1. Therefore, the two materials were simultaneously sputtered, and the composition of the thin film was regulated by the size of the openings and the applied powers, as shown in Figure 1 (c)-(d). As the targets are pointed at the substrate perpendicularly, oblique deposition is largely avoided. A similar methodology, referred to as composite targeting, was developed in our previous paper[23] and by other groups[24].

Figure 1(e) shows the Table of $Cu_xAl_{(100-x)}$ compositions calculated from X-ray photoemission spectroscopy (XPS) spectra. The compositions of the mixtures are determined by the size of the openings and the power. Specifically, as the content of Cu increased from 1% to 81%, the opening potential of the topmost Al electrode increased. Subsequently, we reduced the sputtering power, and the concentration of Cu continuously increased to 99%. As shown in Figures S2 and S3, the $Cu3p^{3/2}$ core level of the XPS spectrum is decomposed into two peaks corresponding to Cu^0 (75 eV) and Cu^+ (78 eV). The presence of monovalent Cu^+ ions was further confirmed by X-ray diffraction (XRD) (Figure S4), which suggested that the surface of the $Cu_xAl_{(100-x)}$ electrode was slightly oxidized upon contact with the air.

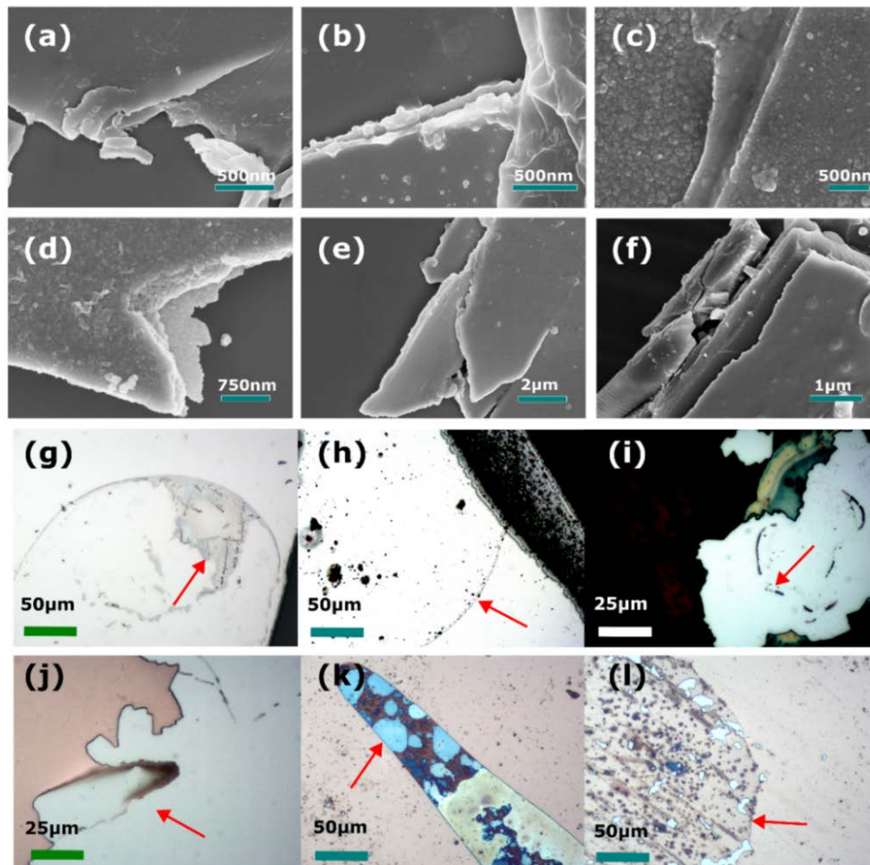

Figure 2 Scanning electron microscopy (SEM) images of (a) $Cu_{0.01}Al_{0.99}$, (b) $Cu_{0.07}Al_{0.93}$, (c) $Cu_{0.19}Al_{0.81}$, (d) $Cu_{0.19}Al_{0.81}$, (e) $Cu_{0.97}Al_{0.03}$, and (f) $Cu_{0.99}Al_{0.01}$. Optical microscopy images of $Cu_xAl_{(100-x)}$ freestanding flakes after exfoliation (the red arrow points at the boundary of the flakes): (g) $Cu_{0.01}Al_{0.99}$, (h) $Cu_{0.07}Al_{0.93}$, (i) $Cu_{0.19}Al_{0.81}$, (j) $Cu_{0.19}Al_{0.81}$, (k) $Cu_{0.97}Al_{0.03}$, and (l) $Cu_{0.99}Al_{0.01}$.

Figure 2 shows the surface morphology of 2D $Cu_xAl_{(100-x)}$ after exfoliation. $Cu_xAl_{(100-x)}$ samples were sonicated in a water bath for 5 mins. Freestanding flakes are observed at the edges, as shown in Figure 2(a)-(f). The appearance of the flakes was semitransparent or colorful under an optical microscope, as shown in Figure 2 (g)-(l). In Figure 2(j), the appearance of flakes gradually changes from transparent to dark red with an increase in the number of Cu single layers. Therefore, transparent metals are promising for use, e.g., in photoelectric devices. The flakes in Figure 2 (k) exhibit a common photochromatic surface, which was discussed in our previous paper and was possibly caused by the light interference effect between the flakes and the air.

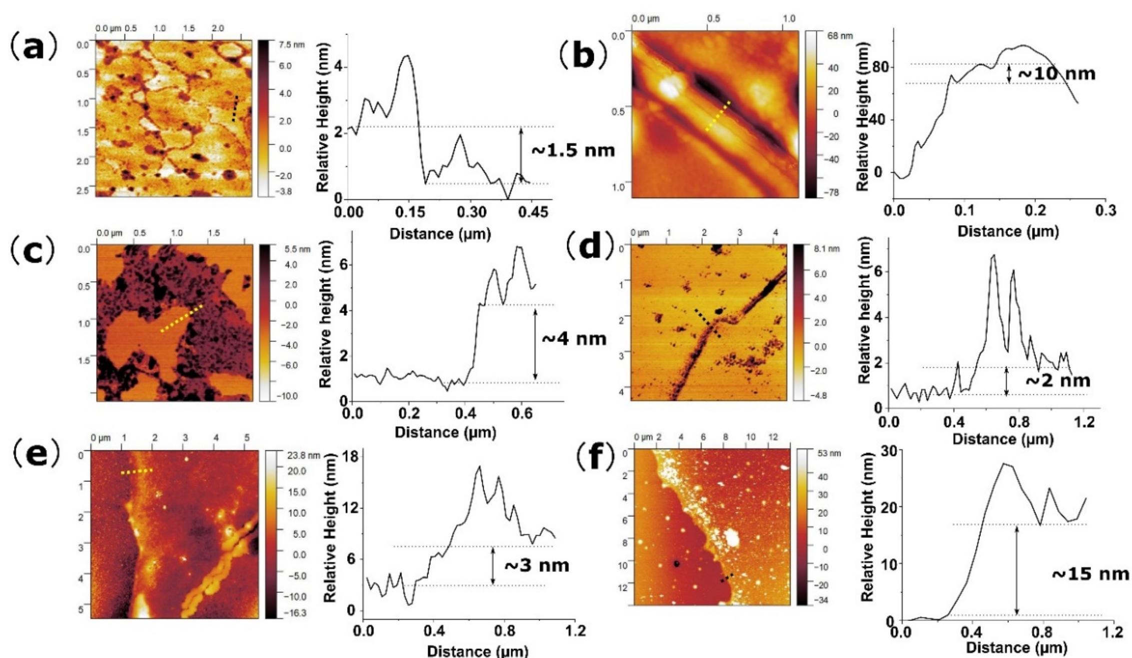

Figure 3 Topographic image and profiles (at the position of the dashed line) of 2D $Cu_xAl_{(100-x)}$ after ultrasonic exfoliation: (a) $Cu_{0.01}Al_{0.99}$, (b) $Cu_{0.07}Al_{0.93}$, (c) $Cu_{0.19}Al_{0.81}$, (d) $Cu_{0.19}Al_{0.81}$, (e) $Cu_{0.97}Al_{0.03}$, and (f) $Cu_{0.99}Al_{0.01}$.

The topography of the freestanding flakes of the $Cu_xAl_{(100-x)}$ samples was obtained using atomic force microscopy (AFM), and the thickness of the freestanding single layer was measured at the edge of the flakes. Since 2D $Cu_xAl_{(100-x)}$ was formed during self-assembly, the thicknesses of the single layers, which varied from 1.5 nm to 15 nm, are shown in Figure 3. The minimum thickness is 1.5 nm, and the ultrathin single layer results in the transparency of the material, as shown in Figure 2. In general, 2D metals are generally difficult to synthesize. [25] Therefore, sputtered two-dimensional metals, which are thinner, larger in lateral size, and transparent, are ideally utilized as interconnects or electrodes in electronic devices.

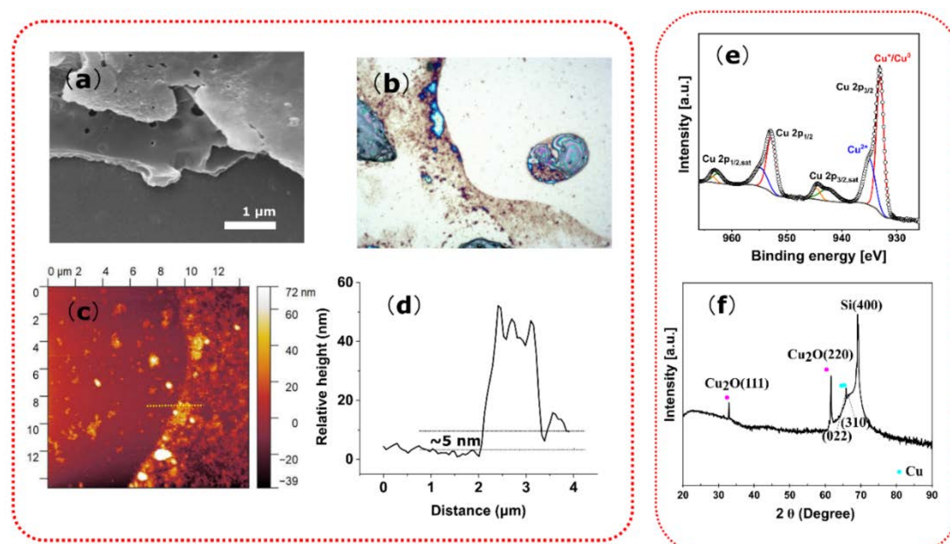

Figure 4 (a) SEM images at the step of the freestanding $Cu_{21}(SiO_2)_{79}$ single layer; (b) optical microscopy image of the freestanding $Cu_{21}(SiO_2)_{79}$ single layer; (c) AFM image of the freestanding $Cu_{21}(SiO_2)_{79}$ single layer; (d) profile from the dashed line in (c); (e) XPS spectrum of the $Cu_{21}(SiO_2)_{79}$; (f) XRD spectrum of the $Cu_{21}(SiO_2)_{79}$ material.

The $Cu_{21}(SiO_2)_{79}$ electrolyte was also synthesized by a similar method, as shown in Figure 1. During deposition, Cu particles

precipitated among the single layers due to the dissolution limit of Cu in SiO_2. Therefore, we utilized $FeCl_3$ acetone solution for the exfoliation of 2D $Cu_{21}(SiO_2)_{79}$. The $FeCl_3$ solution can react with Cu particles and delaminate adjacent single layers. The semitransparent appearance of $Cu_{21}(SiO_2)_{79}$ after exfoliation is similar to that of $Cu_xAl_{(100-x)}$, as demonstrated in Figure 4 (a) and (b). Figure 4(c)-(d) shows the topographic images, where the thickness of the SiO_2 layer is ~5 nm.

The oxidation states of copper in the 2D $Cu_{21}(SiO_2)_{79}$ electrolyte were analyzed using the Cu 2p XPS spectrum in Figure 4e, and the XPS data are presented in Figure S5. The signals of Cu, Cu^+ and Cu^{2+} are obtained after the decomposition of the Cu 2p spectrum. The valence states of Cu are further confirmed from the XRD spectrum, where the peak centered at 36.3° represents the Cu_2O (111) reflection. In summary, these results confirm the precipitation of Cu particles among single layers.

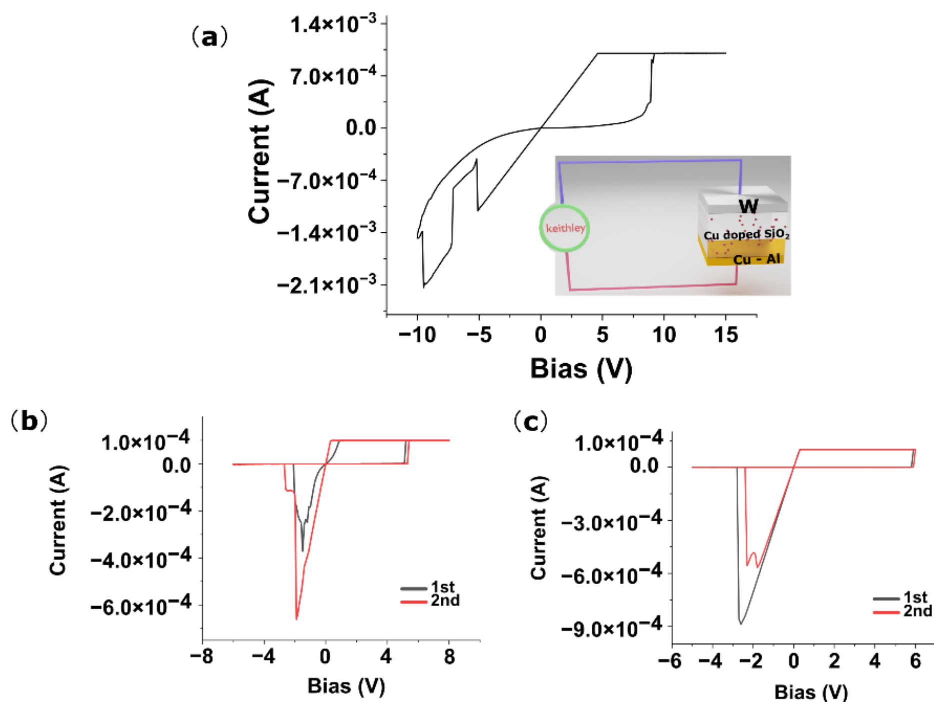

Figure 5 (a) I-V curve of the memristive device with the $Cu_{0.01}Al_{0.99}$ electrode (the inset shows the structure of the $W/Cu_{21}(SiO_2)_{79}/Cu_xAl_{(100-x)}$ memristive device); (b)-(c) I-V curves of the memristive device with the $Cu_{0.19}Al_{0.81}$ and $Cu_{0.99}Al_{0.01}$ electrodes.

Figure 5 shows the resistive switching behavior of the W(TE)/$Cu_{21}(SiO_2)_{79}$/$Cu_xAl_{(100-x)}$(BE) memristive device, in which three compositions of $Cu_xAl_{(100-x)}$ electrodes were fabricated. The electric circuit was plotted as shown in Figure 5(a), where the inert tungsten electrode and active $Cu_xAl_{(100-x)}$ electrodes were connected with a Keithley 2612. During a positive DC sweep, the Cu ions migrate along the electric field and precipitate as conductive filaments (referred to as the SET process). In contrast, conductive filaments are dissolved by Joule heat in a negative DC sweep (referred to as the RESET process).

In this paper, we used 2D $Cu_xAl_{(100-x)}$ electrodes as active electrodes for memristive devices. The inclusion of Al stabilizes the Cu electrode via electromigration. However, the content of Al must be within a suitable range. The memristive device with a $Cu_{0.01}Al_{0.99}$ electrode presented an irregular I-V curve, and only one cycle was obtained, as shown in Figure 5(a). Due to the lack of Cu in the electrode, we believe that filaments are formed with the help of Cu nanoparticles embedded within the $Cu_{21}(SiO_2)_{79}$ electrolyte. The I-V curves in Figure 5(b) and (c) were obtained from memristive devices with $Cu_{0.19}Al_{0.81}$ and $Cu_{0.99}Al_{0.01}$ electrodes, neither of which presented a clear electroforming process. Therefore, the device does not need a noble metal electrode to facilitate the formation of filaments. The stable retention and cycling performance of devices were presented in Figure S6, and Figure S7 (a) and (b). Figure S7 (c) and (d) show the cumulative probability distributions of the SET and RESET biases of both memristive devices over 100 cycles. The instability of the HRS or LRS in some cycles is mostly caused by Joule heating.[26] The average value of the SET bias in the memristive device with the $Cu_{0.19}Al_{0.81}$ electrode is clearly greater than that with the $Cu_{0.99}Al_{0.01}$ electrode. In other words, the SET biases can be regulated via the compositions of the electrodes. In the literature, electrode engineering is often applied to VCM (valence change mechanism)-based memristive devices.[27–30] Our results show the possibility of electrode engineering with CBRAM (conductive-bridging RAM)-type memristive devices. During the formation of conductive filaments, the Cu electrode is constantly oxidized and transformed into Cu ions. Therefore, a lower Cu content within electrodes can result in a higher SET bias threshold. The crystalline structure of the $Cu_xAl_{(100-x)}$ electrode was further studied via TEM imaging, as shown in Figure S8 (a) and (b). As confirmed from the XPS and XRD results, Cu and Al are separated into two distinct phases. As shown in Figure S8 (b), the black region is suggested to be Cu (111). In addition, nanocrystalline Cu contributes to the formation of conductive filaments, as shown in Figure S8 (c).

3 Conclusion

In this paper, a memristive device (W(BE)/$Cu_{21}(SiO_2)_{79}$/ $Cu_xAl_{(100-x)}$(TE)) was fabricated with 2D electrodes and an electrolyte. 2D $Cu_{21}(SiO_2)_{79}$ and $Cu_xAl_{(100-x)}$ were formed via RF magnetron sputtering with modified targets. Generally, electrode engineering is applied to VCM-based memristive devices, which has rarely been discussed in ECM-based memristive devices. In our paper, the SET and RESET biases of ECM-based memristive devices are regulated via the binary compositions of $Cu_xAl_{(100-x)}$ electrodes, where a lower Cu concentration is associated with a higher SET bias. Moreover, the interface of 2D $Cu_xAl_{(100-x)}$ plays an important role in determining the SET and RESET biases. Since both electrodes and electrolytes were fabricated as 2D materials via RF sputtering, a promising application of this synthesis method for 2D materials was shown in the future.

4 Experiment

The devices were fabricated with a classic crossbar configuration consisting of three layers (W(BE)/$Cu_{21}(SiO_2)_{79}$/ $Cu_xAl_{(100-x)}$(TE)), and the size of the cross point was 100 μm × 100 μm. The overall thickness of the $Cu_{21}(SiO_2)_{79}$ layer is 500 nm. The subsequent DC sweep was measured via a Keithley 2600 instrument equipped with probes. In the first step, 2D tungsten was deposited onto a silicon wafer, followed by deposition of a 2D $Cu_{21}(SiO_2)_{79}$ electrolyte via a combination of Cu and SiO_2 targets. 2D $Cu_xAl_{(100-x)}$ as the top electrode was deposited via a combination of Cu and Al targets. The exfoliation of 2D $Cu_xAl_{(100-x)}$ was conducted via sonication in a water bath for 5 mins. The exfoliation of $Cu_{21}(SiO_2)_{79}$ was completed via treatment with a saturated $FeCl_3$ acetone solution. Afterward, the samples were rinsed multiple times with distilled water and transferred to an optical microscope for observation. The details of the surface morphologies were also examined via an SEM S4800 instrument under an acceleration voltage of 10 kV. The height of the steps and topographical images were studied via AFM. XPS was conducted on a Thermo ScientificTM K-AlphaTM$^+$ spectrometer equipped with a monochromatic Al Kα X-ray source (1486.6 eV) operated at 100 W. Samples were analyzed under vacuum ($P < 10^{-8}$ mbar) with a pass energy of 150 eV (survey scans) or 25 eV (high-resolution scans). All the peaks were calibrated with a C1s peak binding energy of 284.8 eV for adventitious carbon. The experimental peaks were fitted with Avantage software. The crystalline structure of the materials was characterized via XRD via a θ-2θ diffractometer (Rigaku Smartlab) using Cu Kα radiation (λ=0.1542).

Acknowledgments
The authors are thankful for the financial support from grants from the Ministry of Education, Youth- and Sports of Czech Republic (grant LM2023037); the European Regional Development Fund Project (NANOMAT CZ.02.1.01/0.0/0.0/17_048/0007376; the Faculty of Chemical Technology, University of Pardubice "Excellent

teams" 2023; the grant from Hebei Normal University (L2021B12); and the HeBei NSF (QN202305).

References

1. Y. Xiao *et al.,* Sci Technol Adv Mater **24**, (2023).
2. P. Zheng *et al.,* Functional Materials Letters **11**, 1850023 (2018).
3. J. Joshua Yang, *et al.,* Nanotechnology **20**, 215201 (2009).
4. U. Celano, *et al.,* Nanoscale **5**, 11187 (2013).
5. S. Dueñas, *et al.,*Microelectron Eng **216**, 111032 (2019).
6. C. Wang, C, *et al.,* Adv Electron Mater **6**, 1901107 (2020).
7. E. W. Lim, *et al.,* J Comput Electron **15**, 602 (2016).
8. S. Liu, *et al.,* Advanced Materials **28**, 10623 (2016).
9. B. Chakrabarti, *et al.,* IEEE Electron Device Letters **35**, 750 (2014).
10. B. Zhang, V. Cicmancova, J. R. Pereira, J. Kupcik, P. Kutalek, and T. Wagner, *et al.,*Appl Surf Sci **530**, 147231 (2020).
11. B. Zhang, *et al.,* Pure and Applied Chemistry **91**, 1787 (2019).
12. B. Zhang, *et al.,*Adv Mater Interfaces **9**, 2201790 (2022).
13. B. Gu, *et al.,* MRS Commun (2024). 10.1557/s43579-024-00529-4
14. H. CHEN *et al.,*Acta Mater **55**, 1617 (2007).
15. Y.-C. Joo, Metals and Materials **4**, 1033 (1998).
16. C. P. Wang *et al.,*J Electron Mater **46**, 4891 (2017).
17. M. Hafner, *et al.,* Physica Status Solidi (a) **210**, 1006 (2013).
18. C. Schindler *et al.,* IEEE T-ED **54**, 2762 (2007).
19. L. Liu, *et al.,* Jpn J Appl Phys **54**, 021802 (2015).
20. N. Ilyas, *et al.,*J Phys Chem Lett **13**, 884 (2022).
21. C.-J. Wang *et al.,* Journal of Physics and Chemistry of Solids **69**, 523 (2008).
22. D.-X. Ye, *et al.,*Nanotechnology **16**, 1717 (2005).
23. B. Zhang, *et al.,*Appl Surf Sci **655**, 159584 (2024).
24. P. C. Akshara *et al.,* Mater Res Express **5**, 036410 (2018).
25. T. Wang *et al.,* Mater Today Adv **8**, 100092 (2020).
26. P. Sun *et al.,* Sci Rep **5**, 13504 (2015).
27. Z. Liao*et al.,*Solid State Electron **72**, 4 (2012).
28. Y. B. Zhu *et al.,*Sci Rep **7**, 43664 (2017).
29. A. Kumar, *et al.,* Semicond Sci Technol **34**, 035014 (2019).
30. Z. Liao *et al.,* Solid State Electron **72**, 4 (2012).